
Preprint:
Akerib, DS, Akerlof, CW, Alqahtani, A et al. (Submitted: 2019) Projected sensitivity of the LUX-ZEPLIN experiment to the 0νββ decay of 136Xe. [Preprint - arXiv]

https://doi.org/10.48550/arxiv.1912.04248

Projected sensitivity of the LUX-ZEPLIN experiment to the $0\nu\beta\beta$ decay of ^{136}Xe

D.S. Akerib,[1,2] C.W. Akerlof,[3] A. Alquahtani,[4] S.K. Alsum,[5] T.J. Anderson,[1,2] N. Angelides,[6] H.M. Araújo,[7] J.E. Armstrong,[8] M. Arthurs,[3] X. Bai,[9] J. Balajthy,[10] S. Balashov,[11] J. Bang,[4] A. Baxter,[12] J. Bensinger,[13] E.P. Bernard,[14,15] A. Bernstein,[16] A. Bhatti,[8] A. Biekert,[14,15] T.P. Biesiadzinski,[1,2] H.J. Birch,[12] K.E. Boast,[17] B. Boxer,[12] P. Brás,[18,a] J.H. Buckley,[19] V.V. Bugaev,[19] S. Burdin,[12] J.K. Busenitz,[20] R. Cabrita,[18] C. Carels,[17] D.L. Carlsmith,[5] M.C. Carmona-Benitez,[21] M. Cascella,[6] C. Chan,[4] N.I. Chott,[9] A. Cole,[15] A. Cottle,[17,22] J.E. Cutter,[10] C.E. Dahl,[23,22] L. de Viveiros,[21] J.E.Y. Dobson,[6] E. Druszkiewicz,[24] T.K. Edberg,[8] S.R. Eriksen,[25] A. Fan,[1,2] S. Fiorucci,[15] H. Flaecher,[25] E.D. Fraser,[12] T. Fruth,[17] R.J. Gaitskell,[4] J. Genovesi,[9] C. Ghag,[6] E. Gibson,[17] M.G.D. Gilchriese,[15] S. Gokhale,[26] M.G.D.van der Grinten,[11] C.R. Hall,[8] A. Harrison,[9] S.J. Haselschwardt,[27] S.A. Hertel,[28] J.Y-K. Hor,[20] M. Horn,[29] D.Q. Huang,[4] C.M. Ignarra,[1,2] O. Jahangir,[6] W. Ji,[1,2] J. Johnson,[10] A.C. Kaboth,[30,11] A.C. Kamaha,[31] K. Kamdin,[15,14] K. Kazkaz,[16] D. Khaitan,[24] A. Khazov,[11] I. Khurana,[6] C.D. Kocher,[4] L. Korley,[13] E.V. Korolkova,[32] J. Kras,[5] H. Kraus,[17] S. Kravitz,[15] L. Kreczko,[25] B. Krikler,[25] V.A. Kudryavtsev,[32] E.A. Leason,[33] J. Lee,[34] D.S. Leonard,[34] K.T. Lesko,[15] C. Levy,[31] J. Li,[34] J. Liao,[4] F.-T. Liao,[17] J. Lin,[14,15] A. Lindote,[18] R. Linehan,[1,2] W.H. Lippincott,[22,b] R. Liu,[4] X. Liu,[33] C. Loniewski,[24] M.I. Lopes,[18] B. López Paredes,[7] W. Lorenzon,[3] S. Luitz,[1] J.M. Lyle,[4] P.A. Majewski,[11] A. Manalaysay,[10] L. Manenti,[6] R.L. Mannino,[5] N. Marangou,[7] M.F. Marzioni,[33] D.N. McKinsey,[14,15] J. McLaughlin,[23] Y. Meng,[20] E.H. Miller,[1,2] E. Mizrachi,[8] A. Monte,[22,b] M.E. Monzani,[1,2] J.A. Morad,[10] E. Morrison,[9] B.J. Mount,[35] A.St.J. Murphy,[33] D. Naim,[10] A. Naylor,[32] C. Nedlik,[28] C. Nehrkorn,[27] H.N. Nelson,[27] F. Neves,[18] J.A. Nikoleyczik,[5] A. Nilima,[33] K. O'Sullivan,[15,14,c] I. Olcina,[7] K.C. Oliver-Mallory,[15,14] S. Pal,[18] K.J. Palladino,[5] J. Palmer,[30] N. Parveen,[31] E.K. Pease,[15] B. Penning,[13] G. Pereira,[18] K. Pushkin,[3] J. Reichenbacher,[9] C.A. Rhyne,[4] Q. Riffard,[14,15] G.R.C. Rischbieter,[31] R. Rosero,[26] P. Rossiter,[32] G. Rutherford,[4] D. Santone,[30] A.B.M.R. Sazzad,[20] R.W. Schnee,[9] M. Schubnell,[3] D. Seymour,[4] S. Shaw,[27] T.A. Shutt,[1,2] J.J. Silk,[8] C. Silva,[18] R. Smith,[14,15] M. Solmaz,[27] V.N. Solovov,[18] P. Sorensen,[15] I. Stancu,[20] A. Stevens,[17] K. Stifter,[1,2] T.J. Sumner,[7] N. Swanson,[4] M. Szydagis,[31] M. Tan,[17] W.C. Taylor,[4] R. Taylor,[7,d] D.J. Temples,[23] P.A. Terman,[36] D.R. Tiedt,[8] M. Timalsina,[9] A. Tomás,[7] M. Tripathi,[10] D.R. Tronstad,[9] W. Turner,[12] L. Tvrznikova,[37,14] U. Utku,[6] A. Vacheret,[7] A. Vaitkus,[4] J.J. Wang,[13] W. Wang,[28] J.R. Watson,[14,15] R.C. Webb,[36] R.G. White,[1,2] T.J. Whitis,[27,1] F.L.H. Wolfs,[24] D. Woodward,[21] X. Xiang,[4] J. Xu,[16] M. Yeh,[26] and P. Zarzhitsky[20]

(The LUX-ZEPLIN (LZ) Collaboration)

[1] *SLAC National Accelerator Laboratory, Menlo Park, CA 94025-7015, USA*
[2] *Kavli Institute for Particle Astrophysics and Cosmology, Stanford University, Stanford, CA 94305-4085 USA*
[3] *University of Michigan, Randall Laboratory of Physics, Ann Arbor, MI 48109-1040, USA*
[4] *Brown University, Department of Physics, Providence, RI 02912-9037, USA*
[5] *University of Wisconsin-Madison, Department of Physics, Madison, WI 53706-1390, USA*
[6] *University College London (UCL), Department of Physics and Astronomy, London WC1E 6BT, UK*
[7] *Imperial College London, Physics Department, Blackett Laboratory, London SW7 2AZ, UK*
[8] *University of Maryland, Department of Physics, College Park, MD 20742-4111, USA*
[9] *South Dakota School of Mines and Technology, Rapid City, SD 57701-3901, USA*
[10] *University of California, Davis, Department of Physics, Davis, CA 95616-5270, USA*
[11] *STFC Rutherford Appleton Laboratory (RAL), Didcot, OX11 0QX, UK*
[12] *University of Liverpool, Department of Physics, Liverpool L69 7ZE, UK*
[13] *Brandeis University, Department of Physics, Waltham, MA 02453, USA*
[14] *University of California, Berkeley, Department of Physics, Berkeley, CA 94720-7300, USA*
[15] *Lawrence Berkeley National Laboratory (LBNL), Berkeley, CA 94720-8099, USA*
[16] *Lawrence Livermore National Laboratory (LLNL), Livermore, CA 94550-9698, USA*
[17] *University of Oxford, Department of Physics, Oxford OX1 3RH, UK*
[18] *Laboratório de Instrumentação e Física Experimental de Partículas (LIP), University of Coimbra, P-3004 516 Coimbra, Portugal*
[19] *Washington University in St. Louis, Department of Physics, St. Louis, MO 63130-4862, USA*
[20] *University of Alabama, Department of Physics & Astronomy, Tuscaloosa, AL 34587-0324, USA*
[21] *Pennsylvania State University, Department of Physics, University Park, PA 16802-6300, USA*
[22] *Fermi National Accelerator Laboratory (FNAL), Batavia, IL 60510-5011, USA*
[23] *Northwestern University, Department of Physics & Astronomy, Evanston, IL 60208-3112, USA*
[24] *University of Rochester, Department of Physics and Astronomy, Rochester, NY 14627-0171, USA*
[25] *University of Bristol, H.H. Wills Physics Laboratory, Bristol, BS8 1TL, UK*
[26] *Brookhaven National Laboratory (BNL), Upton, NY 11973-5000, USA*

[27] University of California, Santa Barbara, Department of Physics, Santa Barbara, CA 93106-9530, USA
[28] University of Massachusetts, Department of Physics, Amherst, MA 01003-9337, USA
[29] South Dakota Science and Technology Authority (SDSTA), Sanford Underground Research Facility, Lead, SD 57754-1700, USA
[30] Royal Holloway, University of London, Department of Physics, Egham, TW20 0EX, UK
[31] University at Albany (SUNY), Department of Physics, Albany, NY 12222-1000, USA
[32] University of Sheffield, Department of Physics and Astronomy, Sheffield S3 7RH, UK
[33] University of Edinburgh, SUPA, School of Physics and Astronomy, Edinburgh EH9 3FD, UK
[34] IBS Center for Underground Physics (CUP), Yuseong-gu, Daejeon, KOR
[35] Black Hills State University, School of Natural Sciences, Spearfish, SD 57799-0002, USA
[36] Texas A&M University, Department of Physics and Astronomy, College Station, TX 77843-4242, USA
[37] Yale University, Department of Physics, New Haven, CT 06511-8499, USA

(Dated: November 25, 2021)

The LUX-ZEPLIN (LZ) experiment will enable a neutrinoless double beta decay search in parallel to the main science goal of discovering dark matter particle interactions. We report the expected LZ sensitivity to ^{136}Xe neutrinoless double beta decay, taking advantage of the significant (>600 kg) ^{136}Xe mass contained within the active volume of LZ without isotopic enrichment. After 1000 live-days, the median exclusion sensitivity to the half-life of ^{136}Xe is projected to be 1.06×10^{26} years (90% confidence level), similar to existing constraints. We also report the expected sensitivity of a possible subsequent dedicated exposure using 90% enrichment with ^{136}Xe at 1.06×10^{27} years.

I. INTRODUCTION

Neutrinoless double beta decay ($0\nu\beta\beta$) is a process by which a nucleus emits two electrons and no neutrinos. This is distinct from two-neutrino double beta decay ($2\nu\beta\beta$), whereby a nucleus emits two electrons and two $\bar{\nu}_e$. $2\nu\beta\beta$ has been observed in several isotopes, and may be observable in even-even nuclei whenever single beta decay is energetically forbidden or highly suppressed [1]. In particular, ^{136}Xe, which comprises 8.9% of naturally occurring xenon, has been shown to undergo $2\nu\beta\beta$ with a half-life of $2.165 \pm 0.016^{(\mathrm{stat})} \pm 0.059^{(\mathrm{sys})} \times 10^{21}$ years with a Q-value of 2457.83 ± 0.37 keV [2, 3]. There are thus far no unambiguous observations of $0\nu\beta\beta$. This neutrinoless decay mode is allowed only if the neutrino is its own antiparticle, an idea originally suggested by Ettore Majorana [4]. Particles which are their own antiparticles are referred to as Majorana particles. A $0\nu\beta\beta$ decay would result in a mono-energetic peak in the β-spectrum at the double beta decay Q-value, $Q_{\beta\beta}$, because the electrons must carry almost all the energy of the decay (with a small fraction going into the recoiling nucleus), allowing one to separate the process from standard model $2\nu\beta\beta$. Observation of $0\nu\beta\beta$ would imply the discovery of fundamental massive Majorana particles, lepton number violation ($\Delta L = 2$), and B–L violation ($\Delta B = 0$ and $\Delta L = 2$). Currently, the best limit on the half-life for $0\nu\beta\beta$ of ^{136}Xe comes from the KamLAND-Zen experiment at 1.07×10^{26} years [5].

A detector designed to observe the $0\nu\beta\beta$ decay of a given source needs to have a complete understanding of the backgrounds in the event search region, a high abundance of the decaying element to compensate for the rare nature of this process and an excellent energy resolution at the Q-value of the decay.

The LUX-ZEPLIN (LZ) experiment features a two-phase xenon time projection chamber (TPC) designed to search for weakly interacting massive particles (WIMPs). While WIMPs present an entirely different signal than $0\nu\beta\beta$, many of the experimental challenges are similar. Both require low backgrounds, a large active mass and, in the case of a xenon TPC, good scintillation and ionization collection. Most $0\nu\beta\beta$ experiments use sources enriched in the isotope of interest, so as to increase the fraction of the relevant isotope and to decrease the passive non-source material. LZ's active detection mass is 7 tonnes of natural liquid xenon (LXe) yielding 623 kg of ^{136}Xe at natural abundance. This is a comparable mass to other world-leading $0\nu\beta\beta$ experiments. Here the sensitivity of LZ to $0\nu\beta\beta$ is investigated and compared to current limits and other next generation $0\nu\beta\beta$ searches using xenon, including nEXO, NEXT, KamLAND2-Zen, and PandaX-III [5–8].

II. THE LZ DETECTOR

A schematic of LZ is shown in Figure 1. LZ will occupy the Davis cavern at the Sanford Underground Research Facility (SURF) in Lead, South Dakota (USA) in the location where the LUX experiment operated from 2012 until 2016 [9–13]. In a two-phase xenon TPC such as LZ, energy deposits produce prompt scintillation light (S1) and free electrons. Some electrons recombine with the xenon ions producing more scintillation light. The electrons that do not recombine drift in an electric field to

[a] Corresponding author: paulo.bras@coimbra.lip.pt
[b] [Now at:]University of California, Santa Barbara, CA 93106-9530, USA
[c] Corresponding author: the.kevin.osullivan@gmail.com; [Now at:]Grammarly, Inc., San Francisco, CA 94104.
[d] Corresponding author: r.taylor16@imperial.ac.uk

the liquid surface where they are extracted into a high-field gas region, creating a proportional scintillation signal (S2) [14–16]. In LZ both signals are detected by two arrays of Hamamatsu R11410-22 3-inch diameter low-radioactivity photomultiplier tubes (PMTs) [17] that observe the active region from the top and bottom: 253 in the top array and 241 in the bottom array. The relative intensity of S2 light in each PMT is used to reconstruct the event position in the horizontal (x,y) plane. The time difference between the S1 and S2 pulses indicates the free electron drift distance and is used to determine the depth (z) of the interaction. The drift field is created by the voltage difference between a cathode grid at the bottom of the detector and a gate grid just below the liquid surface. The electron extraction field around the liquid-gas interface is produced by the voltage applied between the gate grid and the anode grid above the LXe volume. The TPC has a drift region of 145.6 cm (from cathode to gate grid) and an inner diameter of 145.6 cm, and contains 7 tonnes of active xenon. A bottom grid situated below the cathode prevents the bottom PMT array from being exposed to the high fields near the cathode grid. The region between the bottom grid and the cathode grid is 13.75 cm in depth and is referred to as the reverse field region [18].

The TPC is contained inside a low-background, double-walled titanium cryostat [19], containing approximately 10 tonnes of liquid xenon. The TPC is surrounded by an additional volume of xenon instrumented with PMTs, referred to as the xenon "skin". The side section of the skin that surrounds the TPC is 4 cm thick at the top and 8 cm at the level of the cathode. The total amount of xenon in the full skin system is around 2 tonnes. Light collection efficiency of the skin detector is highly dependent on the position of the interaction. Studies of PMT coverage and wall reflectively have led to an expected gamma-ray energy threshold of 100 keV in more than 95% of the skin region.

The cryostat vessel is surrounded by the Outer Detector, containing organic liquid scintillator (gadolinium-loaded linear alkylbenzene), and a water shield. These systems will be viewed by an array of 120 8-inch diameter Hamamatsu R5912 PMTs, providing an additional active veto for gamma-ray scatters in the liquid scintillator. The average light collection efficiency over the entire outer detector volume is estimated to be ∼7%, providing an average light yield of about 130 photoelectrons for a 1 MeV energy deposit in the liquid scintillator [18]. The outer detector system records PMT data in tandem with a triggered event in the LXe TPC, meaning that the energy threshold of the outer detector is only limited by the light collection and the background rate from ^{14}C decay. The prompt coincidence window for the outer detector veto is set as 1 μs for this analysis to reduce the rate of accidental coincidences due to ^{14}C decays in the liquid scintillator (Q-value of 156 keV) in coincidence with a potential $0\nu\beta\beta$ event in the TPC. This coincidence window can be much smaller than that considered for the main WIMP search analysis (500 μs) since neutron interactions are not relevant at the $0\nu\beta\beta$ energies, allowing the threshold of the outer detector to be lowered from 200 keV to 100 keV without increasing the dead time significantly. A more detailed description of the LZ experiment can be found in [18].

A. Event Reconstruction and Energy Resolution

Because the S1 and S2 signals are proportional to the number of scintillation photons and free electrons, each fluctuates due to effects of recombination. Some of the free electrons may recombine, resulting in fewer free electrons and more photons. In this way, for a scatter of fixed energy, there is an anti-correlation between the S1 and S2 signals. Therefore, combining the S1 and the S2 signals to measure deposited energy will substantially improve the energy resolution [20] beyond what may be achieved with the S1 or S2 signals individually.

As the range of energies for a $0\nu\beta\beta$ search is much higher than for dark matter searches, it is expected that some PMT saturation might occur for the S2 signal. A combination of simulation results combined with the PMT voltage divider design indicate that a $0\nu\beta\beta$ S1 will not saturate the PMTs, nor would its S2 saturate the PMTs in the bottom array. However, the S2 will saturate between 7 and 22 PMTs of the top array depending on the drift time and the resulting level of electron diffusion before S2 production. For an S2 signal, approximately 79 photons detected (phd) per extracted electron are assumed with 95% extraction efficiency, with 27 of those photons being detected in the bottom array [21]. As such, the bottom array alone can be used to estimate the S2 size with minimal impact on the energy resolution. However, the top array is used to reconstruct the xy position of events, so the effects of saturation on xy position reconstruction must be considered. The event position is useful for rejecting radioactive backgrounds which are higher in rate at the edge of the detector. The effects of saturation can be minimized by excluding the saturated PMTs from the position reconstruction [22]. Preliminary studies demonstrate that LZ will achieve a xy position resolution of 0.5 cm or better for interaction with deposited energies above 1.8 MeV within a radial distance of 68.8 cm from the center of the detector and across the full drift length of the TPC. Near the center of the detector, the resolution will be 0.2 cm or better.

B. Detector Calibration

The self-shielding provided by liquid xenon makes detector calibration challenging. For this reason, LZ utilizes several radioactive sources that can be injected into the active xenon, which can be removed later or decay away with a short half-life [23, 24]. However, almost all of these sources deposit less than 200 keV in one interaction, making calibration at higher energies more diffi-

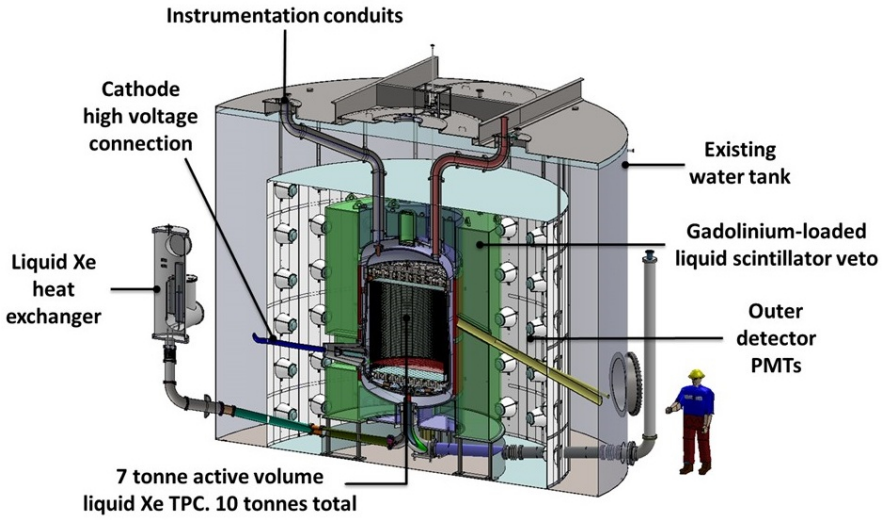

FIG. 1. Schematic of the LZ detector: an outer water tank shields external radioactivity. An outer detector system consisting of a Gd-doped liquid scintillator in acrylic designed to tag outgoing neutrons and gammas is indicated in green. The outer detector is viewed by PMTs to tag energy deposits in the scintillator as well as muons passing through the water tank. The TPC sits inside a titanium cryostat surrounded by the outer detector acrylic tanks. Most of the xenon is contained inside the inner cryostat vessel.

cult. One option is to use a ^{220}Rn source as suggested by [25]. The energy spectrum of the ^{208}Tl daughter has a step around 3.2 MeV created by the coincident beta and gamma decays, and also has alpha decays at 6.2, 6.4, 6.9, and 8.9 MeV. A ^{220}Rn calibration is already planned for LZ, as well as an external ^{228}Th gamma-ray source that will, at the very least, calibrate the outer regions of the active xenon. The internal sources allow for robust correction for the position dependence of the detector response, so performing a high-energy (∼MeV) calibration uniformly through the xenon is not necessary. Lastly, although the backgrounds are very low in the inner volume of the TPC, there is a plethora of visible gamma-ray lines in the outside sections of the active region. Although one would not want to rely on these as the only detector calibration, the LZ background data stands as a useful crosscheck on any high-energy calibration.

III. BACKGROUND MODEL

The main background contributions for this $0\nu\beta\beta$ search are summarized in Table I. Extensive Monte Carlo simulations of the backgrounds due to radioactive contamination in detector components and the cavern rock are generated using BACCARAT, a framework based on GEANT4 that evolved from the LUXSim [26] simulation package, which is also used to make predictions for dark matter sensitivity [21]. The full detector geometry is modeled and matches the engineering drawings. The model used in this analysis was constructed using the most recent material assays and detector simulations [21]. Backgrounds will be measured with high precision once the detector begins the first science run.

There are two important gamma lines to consider for backgrounds near $Q_{\beta\beta}$. There is a line at 2614.5 keV from ^{208}Tl decay in the ^{232}Th decay chain, which is is about 160 keV higher in energy than $Q_{\beta\beta}$ and has a branching ratio of 35.9%. The second, more problematic, gamma line is from ^{214}Bi (^{238}U-chain) at 2447.7 keV with 1.5% branching ratio. This low branching ratio is fortunate, as this line cannot be separated from the signal with the energy resolution of LZ. There is also the possibility of a sum peak from ^{60}Co at $1173.2 + 1332.5 = 2505.7$ keV. However, simulations show that good rejection of multiple scatter events will eliminate this background.

An inner volume was defined with the goal of characterizing the relevant backgrounds for this analysis. This inner volume was optimized using a cut and count analysis and provides a snapshot of the full background model in the most sensitive region of the detector. This volume is defined within $26 < z < 96$ cm and for radii smaller than 39 cm, containing ∼967 kg of LXe. A larger fiducial volume is used for the sensitivity analysis, as discussed in Section IV. The region-of-interest (ROI) considered on this analysis is $2433.3 < E_{dep} < 2482.4$ keV, representing a $\pm$ 1 σ energy window around $Q_{\beta\beta}$, considering an energy resolution (σ/E) of 1% (see Section III A). This energy window is used to characterize the backgrounds in the central $0\nu\beta\beta$ signal region. The sensitivity analysis uses an extended range of energies, from 2000 keV to 2700 keV, in order to model the backgrounds more precisely, as discussed in Section IV.

Figure 2 shows the number of simulated background events in the ROI versus z and radius squared. The back-

TABLE I. Summary table of the masses, activities and estimated background counts in the ± 1 σ ROI and inner 967 kg mass, for a 1000 day run, considering 1.0% energy resolution at Q-value and 0.3 cm multiple scatter rejection along z (see text for details).

Item	Mass (kg)	^{238}U-late (mBq/kg)	Counts from ^{238}U	^{232}Th-late (mBq/kg)	Counts from ^{232}Th	Total Counts
TPC PMTs	91.92	3.22	2.95	1.61	0.10	3.05
TPC PMT bases	2.80	75.87	1.52	33.07	0.03	1.55
TPC PMT structures	165.75	1.60	2.65	1.06	0.12	2.77
TPC PMT cables	88.71	4.31	1.44	0.82	0.19	1.63
Skin PMTs and bases	8.59	45.98	0.75	14.91	0.02	0.78
PTFE walls	184.00	0.04	0.39	0.01	0.00	0.39
TPC sensors	5.02	5.82	1.19	1.88	0.00	1.19
Field grids and holders	89.11	2.63	0.62	1.46	0.11	0.73
Field-cage resistors	0.06	1347.49	2.63	2009.52	0.03	2.65
Field-cage rings	93.02	0.35†	0.82	0.24†	0.00	0.82
Ti cryostat vessel	2594.80	0.08†	1.30	0.22†	0.20	1.49
Cryostat insulation	13.78	11.13†	0.90	7.79†	0.04	0.94
Outer detector system	22 931.46	4.71†	1.70	3.73†	1.08	2.79
Other components	437.68	1.83	2.10	1.65	0.31	2.41
Det. components subtotal	-	-	20.97	-	2.32	23.29
Cavern walls	-	29 000.00	3.21	12 500.00	8.41	11.62
Neutron-induced ^{137}Xe	-	-	-	-	-	0.28*
Internal ^{222}Rn	-	-	-	-	-	0.45*
^{136}Xe $2\nu\beta\beta$	-	-	-	-	-	0.01†
^{8}B solar neutrinos	-	-	-	-	-	0.03
Total	-	-	24.17	-	10.65	35.57

† *Upper limit*
* *preliminary estimate*
^{238} *U-late chain is* ^{226}*Ra and after.* ^{232} *Th-late chain is* ^{224}*Ra and after*

ground rates are higher at the top than at the bottom of the active volume, as the bottom PMTs are shielded by the xenon in the reverse field region. The innermost region of the detector has a much lower background due to the self shielding of LXe. Figure 3 on the left shows the background spectrum for the major contributors, as well as the total background spectrum, for a run lasting 1000 live-days and within the inner 967 kg volume. The right-hand side plot of Figure 3 displays how the successive selection cuts used in this analysis impact the background spectrum in the inner 967 kg volume. A detailed explanation of the selection criteria used in the analysis can be found in Section IV. The "single scatter" selection provides the strongest background rejection for gammas of these energies. However, this analysis cut does not exclude events from the $2\nu\beta\beta$ decay of ^{136}Xe, resulting in the loss of rejection efficiency visible at lower energies on Figure 3.

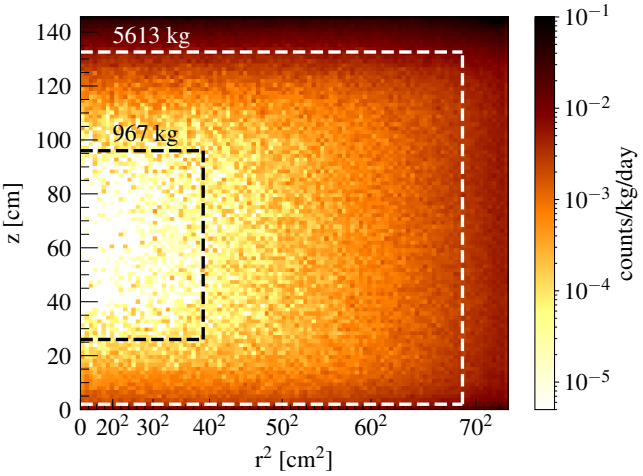

FIG. 2. Background event rate in the active region and in the ± 1 σ energy ROI as a function of r^2 and z. The dashed black rectangle represents the inner 967 kg volume where LZ is most sensitive to the $0\nu\beta\beta$ decay, while the larger dashed white rectangle represents the extended fiducial volume used on the profile likelihood analysis to obtain the LZ sensitivity to the ^{136}Xe $0\nu\beta\beta$ decay.

A. Assumptions About Detector Performance

The energy resolution at the Q-value affects the experiment's ability to reject backgrounds from the 2614.5 keV ^{208}Tl line. Using baseline assumptions about light collection (7.5% photon detection efficiency averaged over the active volume), electron extraction efficiency (95%), and single electron amplification (79 detected photons per extracted e^{-}) for LZ and applying the most recent NEST model, an energy resolution of 0.88% at $Q_{\beta\beta}$ is predicted to be achievable with LZ [28, 29]. XENON1T

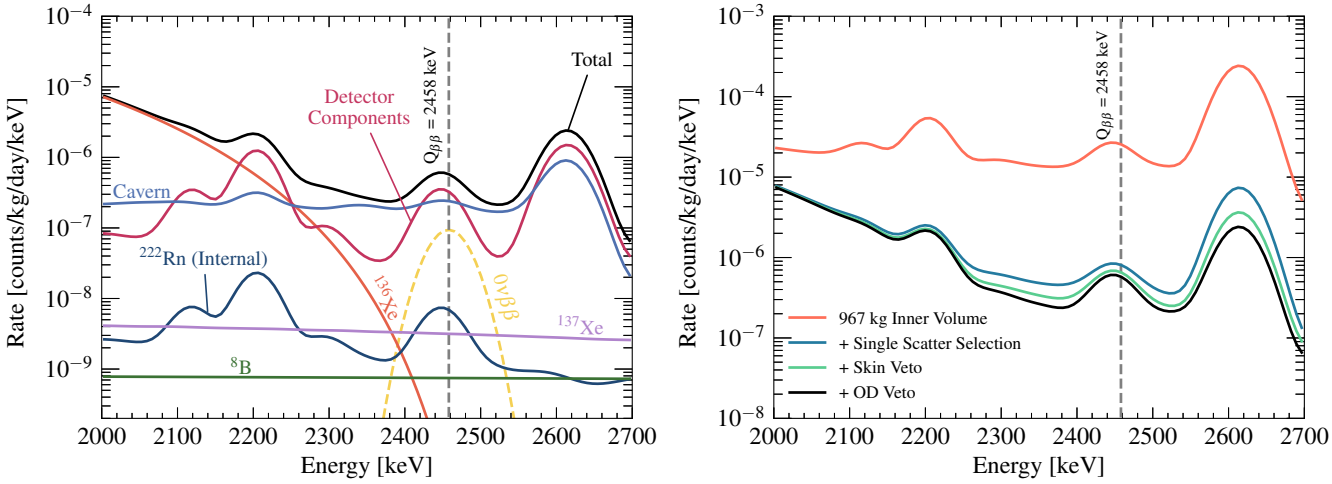

FIG. 3. Background energy spectrum in the inner 967 kg volume: contributions from the main background sources (left) and effect of successive selection cuts used in the analysis (right). More details regarding the analysis can be found in the text. The ^{60}Co, ^{238}U-late chain and ^{232}Th-late chain backgrounds from the detector components are combined into a single curve on the left plot but are treated independently in the sensitivity analysis. The dashed yellow line in the left plot represents the expected signal spectrum for ^{136}Xe $0\nu\beta\beta$ decay, considering a half-life of 1.06×10^{26} years (see Section IV), and it is not included in the total spectrum. The spectra are smeared using the energy resolution function of LUX [27], scaled to be 1.0% at $Q_{\beta\beta}$.

demonstrates that an energy resolution of 0.81% at $Q_{\beta\beta}$ is achievable with a tonne-scale dual-phase xenon detector [30]. The drift field of XENON1T is 80 V/cm, significantly lower than the expected 310 V/cm drift field of LZ [21] and the energy resolution is expected to improve with higher drift field as observed by EXO-200 [31]. An energy resolution of 1.0% at $Q_{\beta\beta}$ is assumed for this analysis, as a conservative value that will likely be improved.

Sensitivity estimates also depend on the minimal vertex separation needed to identify a multiple scatter event. Previous work [32] assumed multiple scatter events could be rejected down to 3 mm separations in z and the same is assumed here. In LZ the full-width at half-maximum of an S2 from a shallow event will be $\sim$1 μs and a drift velocity $\leq$ 2 mm/μs, so in theory separating scatters 2 mm apart should be possible. However, rejecting events with vertex separation in depth less than 3 mm would lower the efficiency for detecting $0\nu\beta\beta$. Diffusion will widen the S2 pulses; this is a known and well-understood Gaussian smearing and can be addressed through advanced analysis, such as applying a drift-time dependent S2 width cut or pulse deconvolution. Vertex separation in xy plane is not used to reject multiple scatter events in this analysis. Preliminary studies show that a vertex separation in the xy plane of 3 cm would only improve background rejection by less than 4% in the inner 967 kg volume.

Finally, any event which deposits more than 100 keV in the LXe skin and/or 100 keV in the outer detector is vetoed. This provides an advantage in tagging the 2614.5 keV ^{208}Tl -line, which is always emitted with another gamma-ray of at least 583 keV. The skin and outer detector are less helpful for reducing the background from the ^{214}Bi line.

B. Detector Components

Every component of the TPC, skin, outer detector and auxiliary systems of LZ is included in the background model. Their individual contributions are estimated using the dedicated BACCARAT simulations mentioned above. Table I summarizes the activities of these components. The categories ^{238}U-late and ^{232}Th-late refer only to the late chain activity, beyond ^{230}Th and ^{228}Th, respectively, as several samples measured by LZ were found to be out of secular equilibrium [18].

All constituent materials have been screened for radioactivity directly by the LZ collaboration in specially designed facilities, with the exception of a few that are based on assay results from previous experiments [33]. Some contamination values for detector materials are measured upper limits. Material assays will continue with the goal of improving the upper limits on several components.

The TPC PMTs are the largest contributor to the backgrounds amongst detector components. The titanium vessels, with a mass of 2.6 tonnes, contributes only half of the total background counts from the full cryostat. Despite the low contamination levels of the outer detector acrylic tanks, the total acrylic mass of 4.3 tonnes is mostly responsible for the background rates from that system. The opposite is true for the resistors, which weigh less than 60 grams combined but have high contamination levels.

C. Davis Cavern Walls

The rock surrounding the Davis cavern is composed primarily of amphibolite and rhyolite [13, 34] that was sprayed with a layer of shotcrete with an average thickness of 12 cm. Recent measurements with a sodium iodide detector in the Davis cavern indicate an average activity of 12.5 Bq/kg of ^{232}Th and of 29.0 Bq/kg of ^{238}U in the surrounding cavern rock [34]. Measurements of gravel from beneath the water tank have shown an activity of 1.7 Bq/kg of ^{232}Th and of 26.3 Bq/kg of ^{238}U [34]. LZ will be shielded from external gamma-rays by a 7.62 m diameter water tank, as well as 6 octagonal steel plates of 5 cm thickness embeded between the concrete and the bottom of the water tank. Although this shielding is more than sufficient for dark matter data taking, an 8 cm thickness of additional steel shielding above the water tank was added to enable a competitive double beta decay analysis. No additional shielding is assumed to be on the sides of the water tank. The outer detector system will be an important tool to mitigate the effect of the gammas from the laboratory rock. In order to tag events from the 2615 MeV line from ^{208}Tl, which is only 160 keV away from the Q-value of the $2\nu\beta\beta$, the outer detector energy threshold is set at 100 keV for this analysis. The outer detector vessels will contain liquid scintillator with a thickness above 60 cm on top, bottom and sides (see Figure 1).

Despite the shielding provided by the several steel plates, scintillator and the water tank, the background from rock gammas is significant. The contributions from the full ^{238}U and ^{232}Th chains were estimated using a detailed set of simulations that included the top and bottom steel plates and both veto systems. The effects of the shielding provided by the top steel plate, water tank, veto systems and detector materials results in a limited number of events reaching the active region and a subsequent loss of efficiency for simulations of sources in the rock. For that reason the same event biasing technique was used as in [18, 34, 35].

Both the ^{238}U and ^{232}Th decay chains have several α emissions with energies up to 8.8 MeV. High energy gammas can be produced in (α, γ) reactions in the rock on oxygen and silicon [36], the most abundant elements in the cavern rock at SURF. Fortunately, the expected flux of these high energy gammas is 2 to 3 orders of magnitude lower than the radiogenic gammas from the ^{238}U and ^{232}Th decay chains, resulting in a total contribution to the background of less than one count in the inner 967 kg volume and in 1000 live-days, despite their high penetrative power.

D. Internal Radon

Radon emanates from detector materials and residual dust in the internal surfaces of the TPC into the liquid bulk. LZ has a requirement of < 2.0 μBq/kg of ^{222}Rn, equivalent to 14 mBq in the active xenon. The current projections conservatively assume emanation at room temperature, whereas emanation from many materials will be decreased at lower temperatures.

One of the daughters of the ^{222}Rn-chain is ^{214}Bi, whose 2448 keV gamma line cannot be separated from the $0\nu\beta\beta$ ROI by energy resolution alone. However, this gamma line is not a problem for events well-centralized in the xenon as it is vetoed by a coincident β decay. With the low charge detection threshold of LZ (50% efficiency at 1.5 keV$_{ee}$) the event will be rejected in >99.97% of decays by coincidence with the β.

A problematic background from radon-induced ^{214}Bi is a naked-β decay, i.e., a β emission without any accompanying γ emission, with a Q-value of 3.27 MeV and branching ratio of 19.1%. At 1.0% energy resolution, 0.5% of ^{214}Bi decays will result in a single-scatter event in the ROI. However, the daughter is ^{214}Po which decays by alpha emission with a 163.6 μs half-life, so can be easily detected and used to veto ^{214}Bi decays in the active xenon. By excluding all events with either an α or dead time in the following 2.5 ms, more than 99.99% of internal ^{214}Bi decays will be rejected. This results in around 0.03 background events per tonne in the ROI.

Some of the ^{222}Rn daughters are positively charged and will be captured on the TPC walls or drift to the cathode, where they can decay and produce a background that cannot be vetoed using a coincident decay. In EXO-200 [37], the internal ^{214}Bi activity in their fiducial volume was found to be only 11.6% of the ^{222}Rn activity. Evidence for this effect has also been seen in LUX [38]. The main source of background generated by this population occurs when both the β particle from ^{214}Bi and the α particle from ^{214}Po are absorbed by the walls or by the cathode grid wires and the 2448 keV γ interacts in the liquid xenon. To study this background, we used the same simulations used to predict the background from the cathode grid with an additional efficiency factor to account for the 25% of events where both the β and α are absorbed by the walls, as well as the fraction of mass inside the active region. If we assume that all the ^{214}Bi drifts to the cathode, we predict around 0.41 events in the inner 967 kg volume from this source in 1000 days. This value can be reduced further by the observation of the recoil signal from ^{210}Pb after the α emission.

E. Internal ^{137}Xe

Muon-induced and radiogenic neutrons can lead to production of ^{137}Xe through the reaction ^{136}Xe(n,γ)^{137}Xe. This isotope is a β-emitter with a Q-value of 4.173 MeV and a half-life of 3.818 minutes, and therefore this β-decay spectrum overlaps with the $0\nu\beta\beta$ ROI. It undergoes a naked β-decay with a branching ratio of 67%.

EXO-200, located at the Waste Isolation Pilot Plant (WIPP) in New Mexico (USA), measured 338^{+132}_{-93} ^{136}Xe(n, γ)^{137}Xe captures per year by fitting data in

coincidence with hits in their muon veto. They calculate that 1.5% of such captures resulted in a background event in their ROI, or $5.1^{+2.0}_{-1.4}$ events per year. The fiducial volume for their analysis contained 76.5 kg of ^{136}Xe [37], implying 70 ROI events/(tonne ^{136}Xe)/year. LZ has three advantages that reduce the muon-induced ^{137}Xe background relative to [39].

1. The muon flux in the Davis cavern is calculated to be 6.2×10^{-9} cm^{-2} s^{-1} [18, 35], nearly 100 times lower than at WIPP (4.0×10^{-7} cm^{-2} s^{-1}).

2. Nearly half of natural xenon is ^{129}Xe or ^{131}Xe , each of which have neutron capture cross sections more than five times larger than ^{136}Xe [40].

3. The LZ detector's large active xenon mass, xenon skin veto, and surrounding outer detector should enable enhanced muon veto efficiency as well as enhanced detection of the neutron capture cascade gamma rays produced in the ^{136}Xe(n,γ)^{137}Xe reaction. By looking back over several ^{137}Xe half-lives for these signatures, potential ^{137}Xe background may be vetoed as in EXO but with higher efficiency.

This results in a factor of 100–1000 fewer events in the ROI per kg of ^{136}Xe compared to EXO-200 [37]. Other muon-induced backgrounds have also been studied and are similarly negligible.

Radiogenic neutrons may also cause ^{137}Xe production through thermal neutron capture. Though the thermal neutron flux is very small within the LZ shielding tank, it is higher outside the shielding, measured to be 1.7×10^{-6} cm^{-2} s^{-1} within the Davis cavern [41]. Xenon within the purification system is exposed to this thermal neutron flux, and given the 4000 kg/day xenon purification rate, 10 kg of xenon is delivered to LZ over the 3.8 minute half-life of ^{137}Xe, about half of which will go into the time projection chamber. This mechanism produces about 0.24 events in the ROI and inner 967 kg volume over the 1000 day exposure. In addition, some ^{137}Xe produced by thermal neutron capture in the purification system will decay in the LXe conduit passing through the shielding tank before reaching the LZ time projection chamber.

F. Other Backgrounds

The two-neutrino decay mode of ^{136}Xe can result in a background in the ROI as it has the same Q-value as $0\nu\beta\beta$. However, the spectrum falls off sharply at the end point. Using the $2\nu\beta\beta$ spectrum taken from [42], for 1.0% energy resolution this results in less than 0.01 background events in 1000 days and in the inner 967 kg volume, or 6.9×10^{-6} events/kg ^{136}Xe/year in the $\pm$ 1 σ ROI. ^{8}B solar neutrinos similarly result in a rate of 0.01 events/tonne/year, corresponding to 0.03 events in the ROI over 1000 days of live time and in the inner 967 kg volume, considering a neutrino flux of 5.79×10^{6} cm^{-2} s^{-1} [43].

IV. SENSITIVITY PROJECTION

The sensitivity to $0\nu\beta\beta$ decay is defined as the median 90% confidence level (CL) upper limit on the number of signal events that would be obtained from a repeated set of background-only experiments, assuming 1000 days of detector live time and a LXe mass of 5.6 tonnes, corresponding to a 1360 kg·years exposure of ^{136}Xe. To estimate the background contribution for such an exposure, a multidimensional background model is constructed that accounts for each of the sources discussed in section III. Each background is described by the three observables: energy ($2000 < E < 2700$ keV), depth ($2 < z < 132.6$ cm) and radial position ($r < 68.8$ cm). These are combined to model the background with a probability density function (PDF) $P(E, r^2, z)$. For the detector, cavern, and internal radon backgrounds, the PDFs are empirically determined from energy deposit simulations and are approximated by decomposing into factorised energy and position distributions $P(E, r^2, z) = P(E)P(r^2, z)$, which has been verified as a suitable approximation in the given ranges of the observables. The following selection criteria are applied to the simulations to reject background events:

- Fiducial Volume: events that occur close to the TPC walls and grids are rejected with a fiducial cut. The extended fiducial volume is defined as 4 cm from the TPC walls, 2 cm above the cathode grid and 13 cm below the gate grid, which defines a region containing 5.6 tonnes of LXe. This cut removes backgrounds which may originate from the grids or TPC walls such as the β-emitting charged ^{222}Rn daughters.

- Single Scatter: ^{136}Xe $0\nu\beta\beta$-decay events in LXe are almost point-like and therefore are expected to produce a single-scatter S2 pulse, whereas the dominant γ-ray background predominantly results in extended, multiple scatter events. These are rejected by requiring that multiple vertices are separated by less than 3 mm in the vertical direction, i.e., $\Delta z < 3$ mm.

- Veto: γ-ray backgrounds that produce a single scatter in the TPC but deposit more than 100 keV either in the outer detector or in the skin vetoes within a narrow 1 μs time window are rejected. This has a significant effect on reducing the background from the ^{208}Tl 2614.5 keV line, which originates from both the detector components and cavern walls.

The remaining backgrounds are expected to have uniform position distributions and are therefore char-

acterised by their energy spectra alone. The ^{136}Xe $2\nu\beta\beta$ decay spectrum is from [42] and the ^{137}Xe β-decay spectrum is obtained from [44]. To model the finite energy resolution, each of the energy distributions are smeared using the LUX energy resolution function [27] that has been scaled to ensure $\sigma/E = 1\%$ at the Q-value.

The ^{136}Xe $0\nu\beta\beta$ signal is modelled with a uniform position distribution and a Gaussian energy distribution centered at $Q_{\beta\beta}$. The signal efficiency is estimated to be 80% after simulating signal events with initial kinematics generated using DECAY0 [45] and applying the selection criteria. The inefficiency is due to the rejection of multiple scatter signal events arising from Bremsstrahlung emission.

The signal and background PDFs are combined to form the unbinned extended likelihood function,

$$L(\mu_s, \{\mu_b\}) = \left[\mu_s P_s(E, r^2, z) + \sum_{i=1}^{n_b} \mu_b^i P_b^i(E, r^2, z)\right] \prod_{j=1}^{n_b} g(a_b^j, \sigma_b^j), \quad (1)$$

where the floating parameters are μ_s, the number of signal events, and μ_b^i, the number of events for the i-th background source. The systematic uncertainties σ_b^j on the expected background rates a_b^j are included by treating the background sources as nuisance parameters with the set of Gaussian constraint terms $g(a_b^j, \sigma_b^j)$. Table II summarises the background sources included as parameters in the likelihood as well as the relative systematic uncertainties on their rate. The uncertainties on the detector component background rates are estimated from simulation and those on the cavern background are from the uncertainty of the measured ^{232}Th and ^{238}U activities [34]. The uncertainty for the ^{222}Rn component is driven by the range of the estimated contamination and those for ^{136}Xe and ^{8}B come from half-life and flux uncertainties, respectively. Finally, the internal ^{137}Xe background and ^{214}Bi cathode background are assigned a large uncertainty as their true rates will not be known until measured. However these are minor backgrounds and therefore do not significantly affect the sensitivity.

The 90% CL upper limit on the number of signal events is calculated using the profile likelihood ratio (PLR) method, utilising the asymptotic one-sided profile likelihood test-statistic [46]. It has been verified that Wilk's theorem is valid and that the asymptotic approximation is applicable.

The sensitivity analysis takes advantage of the precise multi-parameter reconstruction of events in the LXe TPC, namely the energy and 3-dimensional position, for enhanced sensitivity. As demonstrated by Figure 2, the self shielding LXe of LZ results in a low background inner region of the TPC where the majority of signal sensitivity is expected. However, the analysis utilises an extended fiducial volume which allows for the fit of the backgrounds close to the TPC walls and therefore constrains the background in the inner volume of the TPC.

TABLE II. Summary table of the individual background sources and the relative uncertainties on their background rates assumed in this analysis.

Background	σ/N
^{238}U (Detector)	30%
^{232}Th (Detector)	30%
^{60}Co (Detector)	30%
^{238}U (Cavern)	50%
^{232}Th (Cavern)	30%
^{214}Bi (Cathode)	50%
^{222}Rn (Internal)	50%
^{137}Xe (Internal)	50%
^{136}Xe $2\nu\beta\beta$	5%
^{8}B solar ν	5%

Alongside this, the full shape of the position distribution can be used to discriminate between signal-like and background events, which results in both increased signal exposure and sensitivity compared to a simple cut based analysis. Similarly, the extended energy range used in the PDFs strongly constrains the backgrounds near the Q-value. Using an extended phase-space in the profile likelihood analysis improves the sensitivity result by a factor of two when compared to a simple cut and count analysis.

A. Projection with Natural Abundance of ^{136}Xe

The 90% CL sensitivity to the ^{136}Xe $0\nu\beta\beta$ half-life as a function of detector live time is shown in Fig. 4. A median sensitivity to a half-life of 1.06×10^{26} years is reached after 1000 live-days.

As the ability to distinguish signal events from the neighbouring ^{214}Bi and ^{208}Tl peaks relies heavily on the energy resolution, the dependence of the sensitivity on the energy resolution at the ^{136}Xe Q-value is shown in Figure 5. It is clear that an energy resolution slightly worse than the assumed 1.0% has a minor impact on the sensitivity. However, if the energy resolution were 2.0% or larger, the impact from the ^{208}Tl peak would be significant.

It is assumed in this analysis that multiple scatter events can be rejected with a depth-based vertex separation cut, as multiple energy deposits at different depths in the TPC will have multiple S2 pulses. As expected, Figure 6 demonstrates that there is a large variation in sensitivity with this cut as multiple scatter events form the dominant background contribution.

Under the assumption that light neutrino exchange is the driving mechanism for $0\nu\beta\beta$, the half-life sensitivity can be translated into the sensitivity to the effective neutrino mass $\langle m_{\beta\beta}\rangle$ through the relation [48]

$$\left(T_{1/2}^{0\nu}\right)^{-1} = \frac{\langle m_{\beta\beta}\rangle^2}{m_e^2} G^{0\nu} |M^{0\nu}|^2. \quad (2)$$

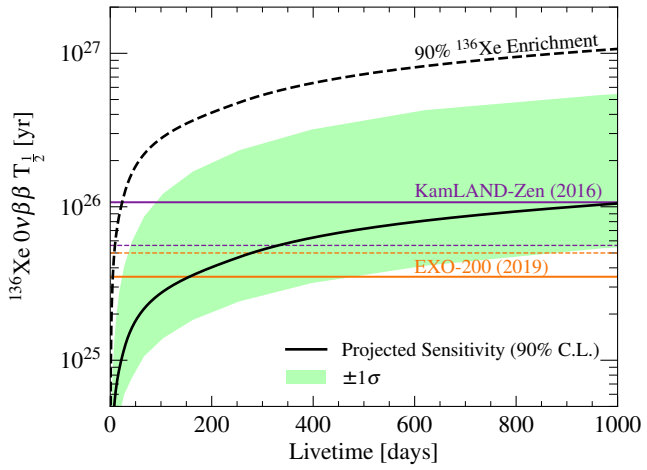

FIG. 4. LZ projected sensitivity to ^{136}Xe $0\nu\beta\beta$ decay as a function of detector live time. The light green shaded band represents a ± 1 σ statistical uncertainty on the sensitivity. The dashed black line shows the projected sensitivity to ^{136}Xe $0\nu\beta\beta$ decay for a dedicated run with 90% ^{136}Xe enrichment. For comparison, the limits set by EXO-200 [47] (orange full) and KamLAND-Zen [5] (purple full) are also shown, along with the respective projected sensitivities (dashed).

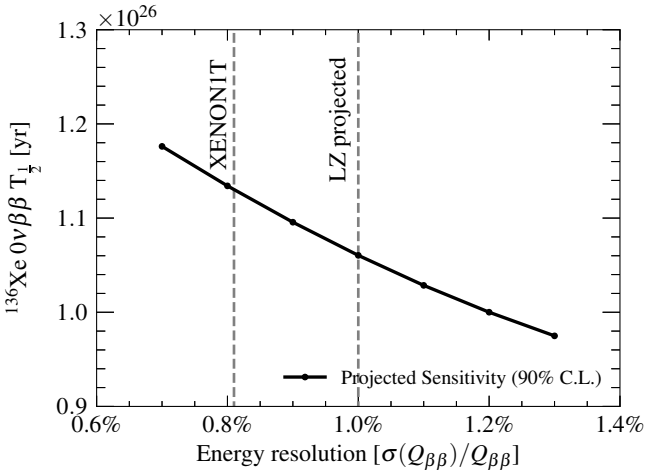

FIG. 5. Expected 90% CL sensitivity for a 1000 live-days run and for various assumed values of energy resolution at $Q_{\beta\beta}$. The vertical dashed line labeled "LZ projected" marks the assumed resolution for this analysis. Also shown on the plot is the projected LZ sensitivity assuming the energy resolution recently measured in XENON1T [30].

Fig. 7 shows that the expected sensitivity to $\langle m_{\beta\beta} \rangle$ after 1000 days is 53–164 meV, with the uncertainty driven by the range of estimates used for the nuclear matrix element [49, 50]. The phase space factor from [42] and an unquenched axial-vector coupling constant of $g_A = 1.27$ are used to calculate the effective neutrino mass.

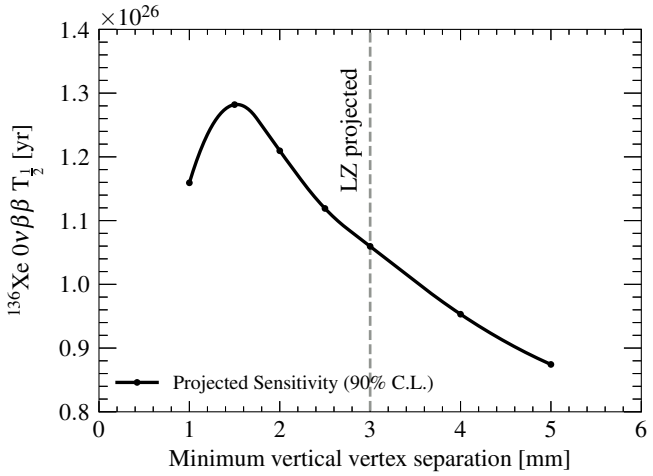

FIG. 6. Expected 90% CL sensitivity for a 1000 live-days run and for various assumed minimum separable vertex distances in depth. Here multiple scatter events are assumed to be rejected based on z separation only. The vertical dashed line marks the assumed separation of 3 mm. At lower separation values, this cut also begins to exclude signal events, resulting in the observed loss in sensitivity.

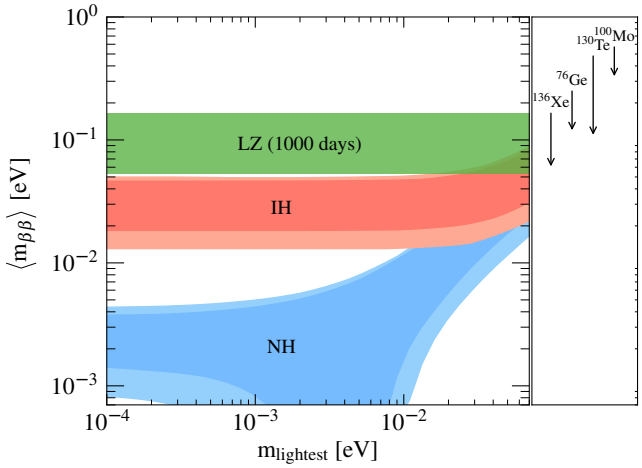

FIG. 7. LZ projected sensitivity to $\langle m_{\beta\beta} \rangle$ and subsequently the neutrino mass hierarchy. The width of the green sensitivity band is due to the uncertainty in the nuclear matrix elements [49][50]. The red and blue contours show the allowed parameter space ($\pm$ 1 σ) for the inverted hierarchy and normal hierarchy neutrino mass scenarios, respectively [6]. On the right are the current best limits and their uncertainties for different $2\nu\beta\beta$ isotopes, showing that ^{136}Xe provides the most stringent constraints on $\langle m_{\beta\beta} \rangle$ [48].

B. Projection with 90% ^{136}Xe Enrichment

After completion of the WIMP-search run of LZ, the sensitivity for $0\nu\beta\beta$ could be extended with several specific upgrades that would be either unnecessary or dis-

advantageous for a dark matter search. The simplest version would be simply to fill the same detector with enriched xenon with no additional upgrades over the WIMP search run. However, with more ^{136}Xe in the active volume of the detector some backgrounds specific to this isotope would increase and need to be accounted for, namely ^{137}Xe production from thermal neutron capture and the $2\nu\beta\beta$ decay of ^{136}Xe. With 1.0% energy resolution the additional background from $2\nu\beta\beta$ would still be negligible and is expected not to impact the sensitivity significantly. Mitigation of the ^{137}Xe background would require the installation of a neutron shield around portions of the xenon purification system. With sufficient shielding this background would also not impact the sensitivity to $0\nu\beta\beta$ significantly. The impact of shielding the LXe conduits outside of the water tank on the production of ^{137}Xe will be studied in more detail in a dedicated analysis. Figure 4 demonstrates that with 90% enriched xenon the sensitivity for a 1000 day run would reach 1.06×10^{27} years.

V. CONCLUSIONS

LZ will be a multi-purpose experiment, capable of exploring a plethora of rare-event phenomena beyond dark matter search due to its ultra-low background environment, great background discrimination potential, large active target mass and an excellent energy resolution.

The LZ experiment will search for $0\nu\beta\beta$ decay with a projected median 90% CL exclusion sensitivity of 1.06×10^{26} years for the half-life of ^{136}Xe, and a sensitivity to $\langle m_{\beta\beta}\rangle$ of 53–164 meV. This result assumes 1% energy resolution at the Q-value of $0\nu\beta\beta$ decay and 3 mm vertex separation in depth. The expected background rate within the $\pm$ 1 σ ROI around the Q-value of $0\nu\beta\beta$ and in an inner 967 kg fiducial volume is about 35 events in 1 000 days of live time. The profile likelihood method benefits from background constraints that result from using a larger volume and energy range. This sensitivity result demonstrates the potential of a two-phase LXe TPC for searching for $0\nu\beta\beta$, as a competitive sensitivity can be reached even for an experiment primarily designed for WIMP detection.

It would be possible, with no improvements in detector parameters and proper mitigation of the ^{137}Xe neutron-induced background, for LZ to conduct a dedicated post WIMP search run with enriched ^{136}Xe that would lead to a sensitivity of 1.06×10^{27} years.

ACKNOWLEDGMENTS

The research supporting this work took place in whole or in part at the Sanford Underground Research Facility (SURF) in Lead, South Dakota. Funding for this work is supported by the U.S. Department of Energy, Office of Science, Office of High Energy Physics under Contract Numbers DE-AC02-05CH11231, DE-SC0020216, DE-SC0012704, DE-SC0010010, DE-AC02-07CH11359, DE-SC0012161, DE-SC0014223, DE-FG02-13ER42020, DE-SC0009999, DE-NA0003180, DE-SC0011702, DESC0010072, DE-SC0015708, DE-SC0006605, DE-FG02-10ER46709, UW PRJ82AJ, DE-SC0013542, DE-AC02-76SF00515, DE-SC0019066, DE-AC52-07NA27344, & DOE-SC0012447. This research was also supported by U.S. National Science Foundation (NSF); the U.K. Science & Technology Facilities Council under award numbers, ST/M003655/1, ST/M003981/1, ST/M003744/1, ST/M003639/1, ST/M003604/1, and ST/M003469/1; Portuguese Foundation for Science and Technology (FCT) under award numbers PTDC/FIS-PAR/28567/2017; the Institute for Basic Science, Korea (budget numbers IBS-R016-D1); University College London and Lawrence Berkeley National Laboratory thank the U.K. Royal Society for travel funds under the International Exchange Scheme (IE141517). We acknowledge additional support from the Boulby Underground Laboratory in the U.K., the GridPP Collaboration [51, 52], in particular at Imperial College London and additional support by the University College London (UCL) Cosmoparticle Initiative. This research used resources of the National Energy Research Scientific Computing Center, a DOE Office of Science User Facility supported by the Office of Science of the U.S. Department of Energy under Contract No. DE-AC02-05CH11231. The University of Edinburgh is a charitable body, registered in Scotland, with the registration number SC005336. The assistance of SURF and its personnel in providing physical access and general logistical and technical support is acknowledged.

[1] R. Saakyan. Two-Neutrino Double-Beta Decay. *Ann. Rev. Nucl. Part. Sci.*, 63:503–529, 2013.

[2] J. B. Albert et al. Improved measurement of the $2\nu\beta\beta$ half-life of ^{136}Xe with the EXO-200 detector. *Phys. Rev. C*, 89:015502, 2014.

[3] M. Redshaw, E. Wingfield, J. McDaniel, and E. Myers. Mass and Double-Beta-Decay Q-Value of ^{136}Xe. *Phys. Rev. Lett.*, 98:053003, 2007.

[4] E. Majorana. Teoria simmetrica dell'elettrone e del positrone. *Nuovo Cim.*, 171, 1937.

[5] A. Gando et al. Search for Majorana Neutrinos near the Inverted Mass Hierarchy Region with KamLAND-Zen. *ArXiv e-prints*, 2016. arxiv:1605.02889.

[6] J. B. Albert et al. Sensitivity and Discovery Potential of nEXO to Neutrinoless Double Beta Decay. *Phys. Rev.*, C97(6):065503, 2018.

[7] J. Martín-Albo et al. Sensitivity of NEXT-100 to Neutrinoless Double Beta Decay. *JHEP*, 05:159, 2016.

[8] Xun Chen et al. PandaX-III: Searching for neutrinoless double beta decay with high pressure^{136}Xe gas time projection chambers. *Sci. China Phys. Mech. Astron.*, 60(6):061011, 2017.

[9] Kevin T. Lesko et al. Deep Underground Science and Engineering Laboratory - Preliminary Design Report. *arXiv [1108.0959] (physics.geo-ph)*, 2011.

[10] Kevin T. Lesko. The Sanford Underground Research Facility at Homestake. *Eur. Phys. J. Plus 127: 107*, 2012.

[11] D. Mei, C. Zhang, K. Thomas, and F. Gray. Early results on radioactive background characterization for Sanford Laboratory and DUSEL experiments. *Astroparticle Physics*, 34:33–39, 2010.

[12] F.E. Gray, C. Ruybal, J. Totushek, D. Mei, K. Thomas, and C. Zhang. Cosmic ray muon flux at the Sanford Underground Laboratory at Homestake. *Nuc Inst and Methods*, 638(1):63–66, 2011.

[13] K.T. Lesko. The Sanford Underground Research Facility at Homestake (SURF). *Physics Procedia*, 61:542–551, 2015. 13th International Conference on Topics in Astroparticle and Underground Physics, TAUP 2013.

[14] B. A. Dolgoshein, V. A. Lebedenko, and B. U. Rodionov. New Method of Registration of Ionizing-particle Tracks in Condensed Matter. *JETP Lett.*, 11:351, 1970.

[15] P. Benetti et al. Detection of energy deposition down to the keV region using liquid xenon scintillation. *Nucl. Instrum. Meth. A*, 327(1):203 – 206, 1993.

[16] V. Chepel and H. Araújo. Liquid noble gas detectors for low energy particle physics. *JINST*, 8:R04001, 2013.

[17] D.S. Akerib et al. An ultra-low background PMT for liquid xenon detectors. *Nuc. Inst. and Methods A*, 703:1–6, 2013.

[18] B. J. Mount et al. LUX-ZEPLIN (LZ) Technical Design Report. *arXiv:1703.09144 (physics.ins-det)*, 2017.

[19] D.S. Akerib et al. Identification of radiopure titanium for the LZ dark matter experiment and future rare event searches. *Astroparticle Physics*, 96:1–10, 2017.

[20] E. Conti et al. Correlated fluctuations between luminescence and ionization in liquid xenon. *Phys. Rev. B*, 68:054201, 2003.

[21] D. S. Akerib et al. Projected WIMP Sensitivity of the LUX-ZEPLIN (LZ) Dark Matter Experiment. *arXiv:1802.06039 (astro-ph.IM)*, 2018.

[22] D. S. Akerib et al. Position Reconstruction in LUX. *JINST*, 13(02):P02001, 2018.

[23] D. S. Akerib et al. Tritium calibration of the LUX dark matter experiment. *Phys. Rev.*, D93(7):072009, 2016.

[24] D. S. Akerib et al. Calibration, event reconstruction, data analysis, and limit calculation for the LUX dark matter experiment. *Phys. Rev.*, D97(10):102008, 2018.

[25] R.F. Lang et al. A ^{220}Rn source for the calibration of low-background experiments. *Journal of Instrumentation*, 11(04):P04004, 2016.

[26] D.S. Akerib et al. LUXSim: A component-centric approach to low-background simulations. *Nucl. Inst. Meth. in Phys. Res. A*, 675:63–77, 2012. doi:10.1016/j.nima.2012.02.010.

[27] D. S. Akerib et al. Signal yields, energy resolution, and recombination fluctuations in liquid xenon. *Phys. Rev. D*, 95:012008, 2017.

[28] M. Szydagis, N. Barry, K. Kazkaz, J. Mock, D. Stolp, M. Sweany, M. Tripathi, S. Uvarov, N. Walsh, and M. Woods. NEST: a comprehensive model for scintillation yield in liquid xenon. *Journal of Instrumentation*, 6(10):P10002, 2011. doi:10.1088/1748-0221/6/10/P10002.

[29] M Szydagis, A Fyhrie, D Thorngren, and M Tripathi. Enhancement of NEST capabilities for simulating low-energy recoils in liquid xenon. *Journal of Instrumentation*, 8(10):C10003, 2013.

[30] Fei Gao. The Energy Linearity and Resolution Performance of the XENON1T two-phase Xenon Time Projection Chamber in the keV to MeV Range, 2019.

[31] G. Anton et al. Measurement of the scintillation and ionization response of liquid xenon at MeV energies in the EXO-200 experiment. *arXiv:1908.04128*, 2019.

[32] L. Baudis et al. Neutrino physics with multi-ton scale liquid xenon detectors. *Journal Cosm Astropart Phys*, 2014(01):044, 2014.

[33] LUX-ZEPLIN Collaboration. "description of and results from the lux-zeplin radio-contaminant control program". in preparation.

[34] D. S. Akerib et al. Measurement of the Gamma Ray Background in the Davis Cavern at the Sanford Underground Research Facility. *Astropart. Phys.*, 116:102391, 2020.

[35] LUX-ZEPLIN Collaboration. Simulations of Events for the LUX-ZEPLIN (LZ) Dark Matter Experiment. in preparation.

[36] A. Tiwari, C. Zhang, D. M. Mei, and P. Cushman. Observation of annual modulation induced by γ rays from (α, γ) reactions at the Soudan Underground Laboratory. *Phys. Rev.*, C96(4):044609, 2017. [Erratum: Phys. Rev.C98,no.1,019901(2018)].

[37] J. B. Albert et al. Measurements of the ion fraction and mobility of α- and β-decay products in liquid xenon using the EXO-200 detector. *Phys. Rev. C*, 92:045504, 2015.

[38] D.S. Akerib et al. Radiogenic and muon-induced backgrounds in the LUX dark matter detector. *Astroparticle Physics*, 62:33–46, 2015.

[39] J.B. Albert et al. Cosmogenic backgrounds to $0\nu\beta\beta$ in EXO-200. *Journal of Cosmology and Astroparticle Physics*, 2016(04):029, 2016.

[40] K. Ni, R. Hasty, T.M. Wongjirad, L. Kastens, A. Manzur, and D.N. McKinsey. Preparation of neutron-activated xenon for liquid xenon detector calibration. *Nuclear Instruments and Methods in Physics Research Section A: Accelerators, Spectrometers, Detectors and Associated Equipment*, 582(2):569–574, 2007.

[41] A. Best et al. Low energy neutron background in deep underground laboratories. *Nuclear Instrumentation and Methods A*, 812:1–6, 2015.

[42] J. Kotila and F. Iachello. Phase-space factors for double-β decay. *Phys. Rev. C*, 85:034316, 2012.

[43] John N. Bahcall, Aldo M. Serenelli, and Sarbani Basu. New Solar Opacities, Abundances, Helioseismology, and Neutrino Fluxes. *The Astrophysical Journal*, 621(1):L85–L88, 2005.

[44] Xavier Mougeot. Betashape: A new code for improved analytical calculations of beta spectra. *EPJ Web of Conferences*, 146:12015, 01 2017.

[45] O. A. Ponkratenko, V. I. Tretyak, and Yu. G. Zdesenko. Event generator DECAY4 for simulating double-beta processes and decays of radioactive nuclei. *Physics of Atomic Nuclei*, 63(7):1282–1287, Jul 2000.

[46] Glen Cowan, Kyle Cranmer, Eilam Gross, and Ofer Vitells. Asymptotic formulae for likelihood-based tests

of new physics. *Eur. Phys. J.*, C71:1554, 2011. [Erratum: Eur. Phys. J.C73,2501(2013)].

[47] G. Anton et al. Search for Neutrinoless Double-Beta Decay with the Complete EXO-200 Dataset. *ArXiv e-prints*, 2019. arXiv:1906.02723.

[48] Michelle J. Dolinski, Alan W. P. Poon, and Werner Rodejohann. Neutrinoless Double-Beta Decay: Status and Prospects. *Submitted to: Ann. Rev. Nucl. Part. Phys.*, 2019.

[49] M. T. Mustonen and J. Engel. Large-scale calculations of the double-β decay of ^{76}**Ge**, ^{130}**Te**, ^{136}**Xe**, and ^{150}**Nd** in the deformed self-consistent skyrme quasiparticle random-phase approximation. *Phys. Rev. C*, 87:064302, Jun 2013.

[50] Nuria López Vaquero, Tomás R. Rodríguez, and J. Luis Egido. Shape and pairing fluctuation effects on neutrinoless double beta decay nuclear matrix elements. *Phys. Rev. Lett.*, 111:142501, Sep 2013.

[51] P.J.W. Faulkner et al. GridPP: development of the UK computing Grid for particle physics. *Journal of Physics G: Nuclear and Particle Physics*, 32(1):N1–N20, 2006.

[52] D. Britton et al. GridPP: the UK grid for particle physics. *Phil. Trans. Royal Society A: Mathematical, Physical and Engineering Sciences*, 367, 2009.